Journal Pre-proofs

Solids lateral mixing and compartmentalization in dynamically structured gas-solid fluidized beds

Laurien A. Vandewalle, Victor Francia, Kevin M. Van Geem, Guy B. Marin, Marc-Olivier Coppens

PII: S1385-8947(21)04639-8
DOI: https://doi.org/10.1016/j.cej.2021.133063
Reference: CEJ 133063

To appear in: *Chemical Engineering Journal*

Received Date: 7 August 2021
Revised Date: 3 October 2021
Accepted Date: 14 October 2021

Please cite this article as: L.A. Vandewalle, V. Francia, K.M. Van Geem, G.B. Marin, M-O. Coppens, Solids lateral mixing and compartmentalization in dynamically structured gas-solid fluidized beds, *Chemical Engineering Journal* (2021), doi: https://doi.org/10.1016/j.cej.2021.133063

Solids lateral mixing and compartmentalization in dynamically structured gas-solid fluidized beds

Laurien A. Vandewalle[1]

Victor Francia [2]

Kevin M. Van Geem[1]

Guy B. Marin[1]

Marc-Olivier Coppens[2*]

[1]Ghent University, Laboratory for Chemical Technology, Technologiepark 125, 9052 Gent, Belgium.

[2]University College London, Centre for Nature-Inspired Engineering and Department of Chemical Engineering, Torrington Place, WC1E 7JE London, UK.

*Corresponding author: m.coppens@ucl.ac.uk

Keywords: Structured fluidized bed, pulsation, CFD-DEM, mixing, lateral dispersion

Abstract:

An adequate use of gas pulsation can create an ordered, dynamically structured bubble flow in a bed of Geldart B particles. A structured bed is more homogeneous, responds to external control and is scalable. While earlier studies have focused on describing the self-organization of the gas bubbles, the solid mixing and gas-solid contact patterns have remained unclear. In this work, the solids circulation and mixing behavior in structured and unstructured beds at various pulsation frequencies are compared with a traditional fluidized bed operation. The degree of lateral mixing is hereby quantified through an effective lateral dispersion coefficient extracted from CFD-DEM (discrete element modelling) simulations in a thin fluidized bed system. Mixing shows major quantitative and qualitative differences amongst the investigated cases. The coordinated motion of the gas bubbles wraps the solid flow into a series of compartments with minimal interaction, whereby effective lateral dispersion coefficients are an order of magnitude lower than in an unstructured operation. More importantly, unlike a traditional bed, dispersion in a structured bed is driven by advection and is no longer a diffusive process. Compartmentalization decouples the time scales of micro- and macromixing. Every pulse, the compartments rearrange dynamically, causing a level of local axial mixing that is scale-independent. While further work is necessary to fully understand the compartmentalization at a larger scale, the circulation described here indicates that a dynamically structured bed can provide a tight control of mixing at low gas velocities and a narrower distribution of stresses in the solid phase compared to traditional devices.

1. INTRODUCTION

Gas-solid fluidized beds are used for a variety of processes in the chemical, petroleum, metallurgical, and energy industries. They are chosen because of their excellent heat transfer and mixing characteristics. For catalytic processes, fluidized bed reactors can be preferred over fixed bed reactors because they allow to use smaller catalyst particles and because of the relative ease with which catalysts can be replaced. However, fluidized beds have important disadvantages, namely their difficult scale-up [1] and the prevalence of mass transfer limitations between the dense emulsion phase and the bubbles [2,3]. The latter results in an inefficient use of reactant gas and a reduction of the overall conversion.

Innovative fluidized bed designs consider ways to impose predictable behavior to facilitate scale-up, control and process integration. To control the flow patterns in the bed and increase the efficiency, new degrees of freedom can be introduced in the design, such as the use of internals, a source of external actuation, a modification to the geometry or the use of a centrifugal field. For operation with Geldart B particles, a reduction of the bubble size is often targeted [4], not only to facilitate scale-up, but also to improve interphase transfer and narrow the residence time distributions, which would help to increase selectivity towards desired intermediate products. One of the ways of introducing a certain degree of structure in a fluidized bed is by pulsating the gas supply. In thin fluidized beds, one can create a regular bubble flow by sinusoidally oscillating the gas flow. Under specific conditions, a regular bubble pattern emerges (see Figure 1) [5], whereby the bubbles organize into a triangular lattice characterized by a lateral wavelength (λ) that is independent of the system dimensions [6]. In every pulse, a new array of bubbles forms into the lattice at alternate positions, leading to a subharmonic pattern, i.e., recurring at a lower frequency than the perturbation applied, namely, *f/2*. In the largest systems, an ordered bubble flow survives

up to a height on the order of magnitude of the bed diameter, above which it is destabilized, breaking down into a more chaotic arrangement (not shown in the figure). To scale up the phenomenon observed in a thin pulsed fluidized bed to a larger bed and to optimize the mixing pattern and the gas-solid contact time, a better understanding of the hydrodynamics and transport phenomena is required.

Since the early 1990s, numerical studies based on computational fluid dynamics (CFD) have been increasingly used to provide insights into fluidization, as they allow to study the bed dynamics without disturbing the flow field [7–9]. There are two approaches for modelling gas-solid fluidized systems: the Eulerian-Eulerian approach, i.e., the two-fluid model (TFM), or the Eulerian-Lagrangian approach, i.e., the discrete element method (CFD-DEM). In the former, the fluid and particulate phase are both treated as continuous phases, and the Navier-Stokes equations are solved for both phases. In the latter, only the fluid phase is modelled as a continuum by solving the Navier-Stokes equations, while for the dispersed phase a large number of individual particles is tracked. It has been reported previously that a classic TFM framework fails to predict the experimentally observed regular lattice in a pulsed fluidized bed [10], whereas a bubble pattern can be accurately reproduced with a CFD-DEM approach [11]. Therefore, in the present study, CFD-DEM is selected as the preferred method to study the particle mixing in a pulsed gas-solid fluidized bed.

In a bubbling fluidized bed, mixing of particles is primarily caused by rising gas bubbles. To quantify how quickly particles are mixing in the axial and lateral direction, *effective* axial and lateral dispersion coefficients are used [12]. Understanding and quantifying solids mixing in a fluidized bed is important, because it is the major contributor to heat and mass transfer. Early studies focused on axial dispersion coefficients to assess the degree of axial backmixing, which is, for example, critical to assess the degree of isothermicity in a gas-solid fluidized bed [13–15].

Lateral dispersion was hereby neglected, although it is an equally important input parameter in simple design tools for fluidized bed reactors. Therefore, recent work has dealt with deriving lateral dispersion coefficients [16] in order to provide engineering reactor models of gas-solid fluidized beds with a quantification of the lateral solids mixing, and, by extension, also lateral heat and mass transfer. Available literature focuses primarily on the experimental methods for estimating lateral dispersion coefficients [17–21] based on tracer methods, generally classified as saline, ferromagnetic, thermal, radioactive, carbon or phosphorescent. All these methods have limitations to their accuracy and resolution [22]. The results from thermal tracking can be difficult to interpret because heat is also transferred to the fluid phase and the walls, safety of personnel and equipment are a concern with radioactive tracking methods, and phosphorescent tracking methods are successful only in dilute fluidized beds. Furthermore, all solid tracer techniques require that numerous runs of experiments are carried out to guarantee repeatability of the results, which is not always feasible.

The use of accurately validated simulations to study the solid flow behavior can provide a great level of insight into the solid mixing patterns. However, numerical studies on lateral dispersion in fluidized beds are still scarce. Liu and Chen [23] performed CFD-DEM simulations to evaluate the lateral dispersion coefficient in large-scale fluidized bed combustors. They studied the influence of the bed width on the lateral dispersion coefficient for a wide range of superficial gas velocities and concluded that the lateral dispersion in industrial-scale fluidized beds is much higher than that in lab-scale beds. Farzaneh et al. [24] used a Lagrangian multigrid technique to model fuel mixing in gas-solid fluidized beds. Oke et al. [16,22] investigated lateral solids mixing in gas-solid fluidized beds using CFD-DEM, and found that the lateral mixing is strongly dependent on the applied frictional stress model and the dimensionality of the simulation.

Pulsation of the gas flow and vibration are ways to enhance the performance of fluidized bed reactors and dryers by improving flowability and heat and mass transfer [5,25,26]. To the best of the authors' knowledge, lateral mixing in oscillating systems such as pulsed and vibrated fluidized beds, let alone the more recent dynamically structured systems, has not been quantified, either experimentally or computationally. A recent study investigated dispersion in a pulsed bed creating a periodic dynamic that is partly due to the interaction with the lateral walls in a small, confined space [27]. The authors found solid dispersion in those conditions to be a sub-diffusive process and proposed further work to analyze the behavior of larger beds that are dynamically structured. Since pulsation and vibration allow break-up of long force chains and particle clusters that are restricting flow, one might expect increased lateral dispersion under an oscillating gas flow at the same average superficial velocity. However, a dynamically structured bed operates in a very different regime with gas flow rates oscillating around the minimum fluidization velocity. The response of the bed to periodic cycles of fluidization and collapse results in a far denser system than with operation at a constant gas flow or the more common (unstructured) use of pulsation. In this "dynamically structured" state, a regular bubble flow (see Figure 1) is maintained at large scale, but it is still unclear how this pattern affects the solid circulation, what level of mixing and gas-solid contact time is achieved and whether the responsive bubble flow can be used to manipulate solid mixing. In particular, it is interesting to investigate in more detail whether the solids mixing behavior can be externally controlled by changes in the pulse characteristics.

This work addresses some of these questions by investigating the solid mixing patterns via numerical simulations of a simplified thin fluidized bed validated with experimental bubbling dynamics. The paper is organized as follows. First the formulation of the CFD-DEM model and simulation settings are described, followed by a discussion on the methodology used for the

analysis of the lateral dispersion. Then, the results of the simulations are presented, including the comparison of a traditional operation under constant gas flow with oscillating fluidized beds at different pulsation frequencies and degrees of stability. A summary of the conclusions is given in the final section.

2. EXPERIMENTAL SET-UP

A thin rectangular fluidized bed is used to study a dynamically structured bubbling bed. Figure 2a depicts the setup comprising of a fluidization chamber, 0.45 m × 0.12 m × 0.01 m, and a plenum chamber, both made of Perspex. Ambient air is filtered, dehumidified, and delivered into the fluidization chamber through a sintered metal distributor plate (3 mm grade 07 Sintertech Poral bronze plate). A sinusoidal air flow is obtained using two parallel lines equipped with needle and solenoid valves (200 SLPM). During operation, the needle valve is kept at a constant aperture and the amplitude u_a and frequency f of the air flow signal are controlled by manipulating the solenoid valve. The air mass flow rate is computed from the instantaneous pressure drop over the distributor, which is measured using GE differential sensors, flush with the wall and calibrated with mass flow meters under the same conditions (OMEGA flow meters, 250 SLPM). The chamber is filled to a static bed height of 0.045 m with Jencons-PLS spherical soda-lime Geldart B glass beads with a density of 2500 kg m^{-3} and a size range between 224-250 μm. The measured minimum fluidization velocity u_{mf} is 0.046 m s^{-1}. Experiments and simulations are conducted under an oscillating air superficial velocity u:

$$u = u_{min} + u_a[1 + \sin(2\pi f t)] \quad (1)$$

where f is the frequency of the applied oscillation, u_{min} is the minimum gas superficial velocity and u_a is the amplitude of the pulse. The resulting time-averaged velocity is $\overline{u} = u_{min} + u_a$. Experiments are conducted at a fixed minimum flow velocity u_{min} = 0.02 m s^{-1}, fixed amplitude

u_a = 0.088 m s^{-1} and varying frequency f = 5, 6, 7 Hz. Figure 2b shows examples of the experimentally observed structure and the scale of the numerical simulation box. As described elsewhere [28], when one operates under a structured pulsation there exists a strong correlation between the size of the bubbles and their separation. An increase in frequency results in a decrease of both the bubble size, due to the lower amount of air injected in every pulse, and the bubble separation, since the range of the circulation around each bubble reduces, which causes the organization into a narrower tessellation. Under the present set of particle and bed properties (i.e., size, density, friction factor, bed height), and overall gas flow (u_{min} , u_a), the transition from an alternating single bubble array to a triangular tessellation occurs in the frequency range 5 – 7 Hz. The conditions are selected to identify the possible differences in the axial dispersion of powder in systems with a single array dominated by nucleation and clustering phenomena, and those where multiple bubble arrays interact, i.e., where bubbles survive in the bed during several pulses.

3. MODEL DESCRIPTION

The simulations are performed with the open source CFD-DEM framework CFDEM®coupling v3.8.0 [29]. This package provides a coupling between OpenFOAM v5 [30], and LIGGGHTS v3.8.0 [31]. In the following, an overview is given of the governing equations, constitutive equations, numerical settings, and boundary conditions used in the present work.

3.1. DEM EQUATIONS

In the DEM framework, each particle in the computational domain is tracked in a Lagrangian way, by explicitly solving the force and torque balances that follow from Newton's second law:

$$m_p \frac{d\boldsymbol{u}_p}{dt} = \boldsymbol{F}_{p,n} + \boldsymbol{F}_{p,t} + \boldsymbol{F}_{p,g} + m_p \boldsymbol{g} \tag{2}$$

$$\boldsymbol{I}_p \frac{d\omega_p}{dt} = \boldsymbol{T}_{p,t} \tag{3}$$

Herein, m_p is the mass [kg] of particle p, $\boldsymbol{u}_p$ is its velocity [m s^{-1}], $\boldsymbol{F}_{p,n}$ is the normal inter-particle contact force [N], $\boldsymbol{F}_{p,t}$ is the tangential inter-particle contact force [N], $\boldsymbol{F}_{p,g}$ is the total force [N] exerted by the gas, $\boldsymbol{g}$ the gravitational acceleration [m s^{-2}], $\boldsymbol{I}_p$ the moment of inertia [kg m^2], ω_p the rotational velocity [rad s^{-1}] and $\boldsymbol{T}_{p,t}$ the torque [N m] induced by the tangential inter-particle contact.

Particle collisions are modelled using the soft-sphere approach proposed by Cundall and Strack [32] allowing for particles to overlap slightly in the collision point. Normal and tangential inter-particle contact forces are then modelled using the Hertzian spring-dashpot contact theory. The normal contact force includes an elastic repulsion force and a visco-elastic damping force [33]:

$$\boldsymbol{F}_{p,n} = k_n \boldsymbol{\delta}_n + \gamma_n \boldsymbol{u}_{r,n} \tag{4}$$

The tangential contact force includes a shear force and a tangential damping force [34]:

$$\boldsymbol{F}_{p,t} = k_t \boldsymbol{\delta}_t + \gamma_t \boldsymbol{u}_{r,t} \tag{5}$$

Herein, k_n and k_t are the normal and tangential elastic constants [N m^{-1}], $\boldsymbol{\delta}_n$ and $\boldsymbol{\delta}_t$ are the normal and tangential geometric overlap between the paired particles [m], γ_n and γ_t are the normal and tangential visco-elastic damping constants [N s m^{-1}], and $\boldsymbol{u}_{r,n}$ and $\boldsymbol{u}_{r,t}$ are the normal and tangential component of the relative velocity of the two particles. The following constitutive equations are used for the elastic constants and visco-elastic damping constants:

$$k_n = \frac{4}{3} Y^* \sqrt{r^* \delta_n} \tag{6}$$

$$k_t = 8 G^* \sqrt{r^* \delta_n} \tag{7}$$

$$\gamma_n = -2\sqrt{\frac{5}{6}}\beta\sqrt{\frac{3}{2}k_n m^*} \tag{8}$$

$$\gamma_t = -2\sqrt{\frac{5}{6}}\beta\sqrt{k_t m^*} \tag{9}$$

Herein, Y^* represents the effective Young's modulus [Pa], G^* the effective shear modulus [Pa], r^* the effective particle radius [m], m^* the effective particle mass [kg], and β is a function of the coefficient of restitution, e, given by:

$$\beta = \frac{\ln(e)}{\sqrt{\ln^2(e) + \pi^2}} \tag{10}$$

The total force exerted by the gas, $\boldsymbol{F}_{p,g}$, includes contributions from the drag force, pressure force and viscous force:

$$\boldsymbol{F}_{p,g} = \boldsymbol{F}_{p,d} - V_p \nabla P - V_p \nabla \cdot \boldsymbol{\tau_g} \tag{11}$$

where V_p is the particle volume [m^3], P the gas pressure [Pa] and $\boldsymbol{\tau_g}$ the gas phase stress tensor [Pa]. The drag force $\boldsymbol{F}_{p,d}$ is discussed in Section 3.2.2.

3.2. CFD-DEM COUPLING

3.2.1. Governing equations

The motion of the gas phase is described by the mass continuity and Navier-Stokes equations, which can be written as:

$$\frac{\partial}{\partial t}(\varepsilon_g \rho_g) + \nabla \cdot (\varepsilon_g \rho_g \boldsymbol{u}_g) = 0 \tag{12}$$

$$\frac{\partial(\varepsilon_g \rho_g \boldsymbol{u}_g)}{\partial t} + \nabla \cdot (\varepsilon_g \rho_g \boldsymbol{u}_g \boldsymbol{u}_g) = -\varepsilon_g \nabla P + \nabla \cdot (\varepsilon_g \boldsymbol{\tau_g}) + \varepsilon_g \rho_g \boldsymbol{g} + \boldsymbol{M}_{g,p} \tag{13}$$

Herein, ε_g is the void fraction [-], ρ_g the gas density [kg m^{-3}], $\boldsymbol{u}_g$ the gas velocity [m s^{-1}], P the gas pressure [Pa], $\boldsymbol{\tau_g}$ the gas phase stress tensor [Pa], $\boldsymbol{g}$ the gravitational acceleration [m s^{-2}], and $\boldsymbol{M}_{g,p}$ represents the momentum exchange with the particulate phase [N m^{-3}]. The gas phase stress tensor is given by:

$$\boldsymbol{\tau_g} = \mu_g\left(\nabla \boldsymbol{u}_g + \nabla \boldsymbol{u}_g^T\right) + \left(\lambda_g - \frac{2}{3}\mu_g\right)(\nabla \cdot \boldsymbol{u}_g)\,\boldsymbol{I} \tag{14}$$

where μ_g is the gas phase shear viscosity [Pa s] and λ_g the bulk viscosity [Pa s]. In the present work, the gas phase is assumed incompressible and isothermal, i.e., the density and viscosity are constant and uniform.

A pressure-based solver is used to solve the above equations, using the *Pressure Implicit Split Operator* (PISO) algorithm for pressure-velocity coupling. In this approach an implicit momentum predictor is followed by a series of pressure solutions and velocity correctors [35]. An important step in the CFD-DEM coupling procedure is the calculation of the void fraction. The positions and volumes of the individual particles need to be translated into a volume fraction field, which is defined on a fixed Eulerian grid. The simplest approach to calculate the volume fraction is to take the sum of the volumes of all particles whose centers are located in a given cell, and to divide this by the cell volume. However, in the present work, the so-called 'divided' volume fraction calculation is used, whereby a particle's volume is distributed over all cells that are (partly) covering it. This approach was found to give the best estimation of the minimum fluidization velocity, mainly because particles near the freeboard of the bed are not assigned to a single cell only.

3.2.2. Gas-particle momentum exchange

The interphase momentum exchange is considered to be solely due to drag, whereas lift and virtual mass forces are considered negligible. The drag force is proportional to the slip velocity, i.e., the relative velocity of the gas to the particles, and is calculated individually for each particle. The drag force exerted by the gas on a particle p is given by:

$$\boldsymbol{F}_{p,d} = -\frac{V_p \beta_d}{1-\varepsilon_g}(\boldsymbol{u}_g - \boldsymbol{u}_p) \tag{15}$$

Herein, V_p is the particle volume [m^3], ε_g is the void fraction, β_d is the drag coefficient per unit volume [kg m^{-3} s^{-1}], $\boldsymbol{u}_g$ is the gas velocity [m s^{-1}] in the cell that contains the particle, and $\boldsymbol{u}_p$ is the individual particle velocity [m s^{-1}].

For numerical reasons, the gas-solid momentum exchange term is split in an implicit and an explicit part:

$$\boldsymbol{M}_{g,p} = K_{g,p}(\boldsymbol{u}_g - \langle \boldsymbol{u}_p \rangle) \tag{16}$$

where

$$K_{g,p} = -\frac{\sum_{p=1}^{N} \boldsymbol{F}_{p,d}}{V_{cell}(\boldsymbol{u}_g - \langle \boldsymbol{u}_p \rangle)} \tag{17}$$

Herein, $\langle \boldsymbol{u}_p \rangle$ is the ensemble-averaged particle velocity [m s^{-1}], and V_{cell} is the volume of the computational cell [m^3].

The drag coefficient β_d is typically obtained from empirical correlations. In this work, drag is computed using Gidaspow's model [36], which uses the Wen and Yu [37] correlation in the dilute regions of the bed, and switches to Ergun's law [38] in the dense regions of the bed.

$\varepsilon_g > 0.8$: (18)

$$\beta_d = \frac{3}{4} C_d \frac{\varepsilon_g(1-\varepsilon_g)\rho_g|\boldsymbol{u}_g - \boldsymbol{u}_p|}{d_p} \varepsilon_g^{-2.65}$$

$$C_d = \frac{24}{\varepsilon_g Re_p}\left[1 + 0.15(\varepsilon_g Re_p)^{0.687}\right] \qquad Re_p = \frac{\rho_g|\boldsymbol{u}_g - \boldsymbol{u}_p| d_p}{\mu_g} \tag{19}$$

$\varepsilon_g \leq 0.8$:

$$\beta_d = 150\frac{(1-\varepsilon_g)^2\mu_g}{\varepsilon_g d_p^2} + 1.75\frac{\rho_g(1-\varepsilon_g)|\boldsymbol{u}_g - \boldsymbol{u}_p|}{d_p} \tag{20}$$

3.3. COMPUTATIONAL SETUP

An overview of operating conditions and computational settings is given in Table 1. The physical properties of the gas and the particles are adopted from a previous work by Wu et al. [11], which included a standard validation of the system, setting the Poisson's ratio, ν, to 0.22, and the coefficient of restitution, e, of the glass beads to 0.97 both for inter-particle and wall-particle collisions. An artificially small Young's modulus (10 MPa) was used for the glass beads to avoid a prohibitively small DEM time step [39,40]. This is common practice to speed up DEM simulations, and was previously found not to have a significant impact on the bubble dynamics for non-cohesive particles [41–44]. The angle of repose, θ, was measured experimentally by piling the glass beads on a horizontal surface, and the friction coefficient between particles, μ_{Fr}, was set to 0.35 according to the approximation $\tan(\theta) \approx \mu_{Fr}$ obtained from the Mohr–Coulomb criterion. It was reduced to 0.1 for particle-wall collisions, μ_w.

The bubble pattern characteristics (bubble size and separation) are independent of the width of the computational domain [45]. A width of 0.1 m was chosen, since this is the minimum size to accommodate the formation of two alternating bubbles in a lattice, for the conditions studied in the present work.

The PISO algorithm was used for pressure-velocity coupling in the gas phase. Second-order accurate discretization schemes were used for gradients and divergences, while a first-order Euler implicit scheme was used for temporal discretization. The DEM time step was set to 1×10^{-6} s, which corresponds to approximately $t_c/50$ (t_c denotes the characteristic collision time) and is considered sufficient to describe the collision process [46,47]. The CFD time step of 1×10^{-4} s was found to be sufficient to achieve convergence and accuracy, while still obeying the Courant-Friedrichs-Lewy (CFL) condition at all times.

As described elsewhere [11], the computational cost is reduced by using a narrow computational domain. The operation with a constant gas flow is studied at a typical superficial gas inlet velocity of $2.5\,u_{mf}$. To provide a direct comparison with historical values of the lateral dispersion coefficient, the computational minimum fluidization velocity, equal to 0.056 m s^{-1}, is used as u_{mf} for the system. A sensitivity analysis confirms that sufficient particle motion and mixing is allowed in a domain with a thickness of 0.002 m. Simulations with a domain thickness of 0.002 and 0.004 m show minor differences in the resulting u_{mf}, and both show a lateral dispersion coefficient in quantitative agreement with literature [19,21,48]. Therefore, a 0.002 m thick domain was used for all subsequent simulations.

The choice of drag model, the choice of interpolation schemes, the assumption of monodispersity and the use of a narrower computational domain lead to a discrepancy in the computational u_{mf}, which is ~18% higher than the experimental value, 0.046 m s^{-1}. This discrepancy does, however, not introduce significant errors in the prediction of bubble size and pattern in the oscillating beds. The superficial inlet velocity is implemented as a modified boundary condition, given by Eqn. (1), using the experimental values for the minimum flow velocity u_{min} = 0.02 m s^{-1}, fixed amplitude u_a = 0.088 m s^{-1} and varying frequency f = 5, 6, 7 Hz.

4. ANALYSIS OF LATERAL DISPERSION

Axial and lateral dispersion coefficients are often used in simplified reactor engineering models, to quantify how quickly particles are mixing in a fluidized bed. These are effective diffusivities, lumping together the effects of various mechanisms, such as bubble break-up and coalescence, emulsion drifting and wake transport. Here, the lateral dispersion coefficient in pulsed fluidized beds is derived from detailed CFD-DEM simulations, for later use in surrogate macroscopic models for predicting and scaling up of this type of fluidized beds. The lateral dispersion coefficient is often defined by an equation similar to Fick's law of molecular diffusion [12]:

$$\frac{\partial C}{\partial t} = D_{sr}\frac{\partial^2 C}{\partial x^2} \tag{21}$$

where C represents the particles concentration [particles m^{-3}] and D_{sr} is the lateral dispersion coefficient [m^2 s^{-1}]. The reasoning behind this diffusion-like mechanism for solid mixing is that each particle in a fluidized bed has equal chance of moving to either the left or right side, hence behaving similar to the molecules of a gas [22]. The thin fluidized bed case presented here is a simple modification of the typical case in literature whereby particles migrate between two halves of a 2D domain. In the case presented here, particles migrate outwards from a centrally located compartment defined by analysis of the bubble dynamics. To make the problem one-dimensional, the particle concentration is averaged over the vertical direction, so that it becomes a function of only the horizontal coordinate x. Initially, the particles in part of the bed, corresponding to the lateral positions $x_1 \leq x \leq x_2$, are marked (see Figure 3a) and the concentration profile of these so-called tracer particles is monitored in time. Numerically, the tracer concentration profile can be

obtained from the CFD-DEM simulations by dividing the bed in a number of vertical layers of width δx [m], and calculating the tracer concentration in each layer, as follows:

$$C_t(x,t) = \frac{n_t(x,t)}{\delta x \cdot H \cdot Z} \tag{22}$$

Herein, $n_t(x,t)$ is the number of tracer particles in the layer centered around the lateral position x at time t, and H and Z are, respectively, the domain height [m] and thickness [m]. The lateral dispersion coefficient can be determined by matching the simulated concentration profile $C_t(x,t)$ with the analytical solution of Eqn. (21).

Now the task remains to determine this analytical solution. The initial and boundary conditions characterizing the above setup are (see Figure 3a):

$$C(x,0) = f(x) = \begin{cases} \tilde{C}(x) & x_1 \leq x \leq x_2 \\ 0 & x < x_1 \text{ and } x > x_2 \end{cases} \tag{23}$$

$$\frac{\partial C(x,t)}{\partial x} = 0 \quad x = 0 \text{ and } x = W \tag{24}$$

The solution of the system defined by Eqns. (21), (23) and (24) can be obtained by using Fourier's method of separation of variables. This yields the general solution:

$$C(x,t;D_{sr}) = A_0 + \sum_{n=1}^{\infty} A_n \cos\left(\frac{n\pi}{W}x\right) \exp\left(-D_{sr}\frac{n^2\pi^2}{W^2}t\right) \tag{25}$$

The coefficients A_n follow from substitution of the initial condition, and are calculated as follows:

$$A_0 = \frac{1}{W}\int_0^W f(x)dx = \frac{1}{W}\int_{x_1}^{x_2} \tilde{C}(x)dx \tag{26}$$

$$A_n = \frac{2}{W}\int_0^W f(x)\cos\left(\frac{n\pi}{W}x\right)dx = \frac{2}{W}\int_{x_1}^{x_2} \tilde{C}(x)\cos\left(\frac{n\pi}{W}x\right)dx \tag{27}$$

The integrals in Eqns. (26)-(27) are evaluated numerically. To facilitate parameter fitting, Eqn. (25) is spatially averaged over the lateral positions $x_1 \leq x \leq x_2$. The resulting expression depends only on time and is given by:

$$C_{av}(t;D_{sr}) = \frac{1}{x_2 - x_1}\int_{x_1}^{x_2} C(x,t)dx = A_0 + \sum_{n=1}^{\infty} \frac{A_n}{x_2 - x_1}\left[\sin\left(\frac{n\pi}{W}x_2\right) - \sin\left(\frac{n\pi}{W}x_1\right)\right]\exp\left(-D_{sr}\frac{n^2\pi^2}{W^2}t\right) \quad (28)$$

Similarly, the simulated tracer concentration profile $C_t(x,t)$ is averaged horizontally over the lateral positions $x_1 \leq x \leq x_2$, resulting in the tracer concentration $C_{t,av}(t)$, which only depends on time. The lateral dispersion coefficient is then obtained by least-squares fitting of this simulated tracer concentration $C_{t,av}(t)$ to the analytical expression for $C_{av}(t;D_{sr})$, Eqn. (28). Note that, if the process is purely diffusion driven and Eqn. (21) holds, the obtained dispersion coefficient is independent of the values of x_1 and x_2. Typically in literature, one half of the bed is marked as tracer particles, i.e. $x_1 = 0$ and $x_2 = W/2$, which further simplifies the analytical solution [16,22,23]. However, the general solution of the diffusion equation, as given by Eqns. (25)-(28), allows to use any value for x_1 and x_2.

One must note certain ambiguity in literature as to whether the approximation of the system to a 1D diffusion process retains physical meaning or whether it is purely numerical. In the authors' view, given that the reported coefficients are to be used in surrogate models as "diffusion" or "dispersion" coefficients, Eqn. (21) must be treated as a proper diffusion equation and, therefore, one must follow the approach above to compute concentration. However, this is not the usual definition found in literature for the term "tracer concentration". For practicality and ease to compare with experimentally derived coefficients, most authors [16,22,23] use a void-free tracer concentration or mass fraction Y, defined as the ratio of the number of tracer particles to the total number of particles in each vertical layer:

$$Y_t(x,t) = \frac{n_t(x,t)}{n_{tot}(x,t)} \tag{29}$$

The lateral "dispersion coefficient" is then obtained by fitting the simulated void-free concentration of tracer particles to the analytical solution of the following system (see Figure 3b):

$$\frac{\partial Y}{\partial t} = D'_{sr}\frac{\partial^2 Y}{\partial x^2} \tag{30}$$

$$Y(x,0) = g(x) = \begin{cases} 1 & x_1 \leq x \leq x_2 \\ 0 & x < x_1 \text{ and } x > x_2 \end{cases} \tag{31}$$

$$\frac{\partial Y(x,t)}{\partial x} = 0 \qquad x = 0 \text{ and } x = W \tag{32}$$

In this case, analytical expressions can be obtained for the coefficients A_n using Eqns. (26)-(27). The lateral dispersion coefficients obtained with both methods, D_{sr} and D'_{sr}, will be different. Indeed, Eqns. (21) and (30) are only equivalent under the assumption that the bed density is constant and uniform. This is not the case. Projecting a 3D fluidized bed on a single coordinate ignores the variation in bed density caused by the formation of gas bubbles. Even in a traditional fluidized bed, the time-averaged density shows a certain spatial distribution since bubbles concentrate preferentially in the central area. In a structured system, on the other hand, the bed density follows a much more defined spatial pattern driven by a fixed set of bubble trajectories, which causes the bed density to fluctuate along the x- horizontal direction. Using the void-free concentration of tracer particles Y averages out these phenomena in both time and space, smoothening the otherwise more fluctuating tracer concentration profiles. In the present work, both definitions will be used and compared.

5. RESULTS AND DISCUSSION

5.1. STRUCTURED BUBBLE FLOW

Pulsating the gas supply at well-chosen conditions leads to a subharmonic flow pattern, where bubbles nucleate at a fixed set of positions, alternating every other pulse. Bubbles rise vertically with minimal lateral motion. Figure 4 illustrates how a pattern emerges during one period of the gas oscillation. The phase angle φ is used to describe the pattern evolution during any period (T) of the oscillating gas flow. The phase angle is hereby defined as $\varphi = 2\pi(t - t_0)/T$, with the initial flow time $t_0 = nT$, in which n is an integer. The bubble pattern is a consequence of the creation of dense solid-like structures in the bed. These appear in the wake and between rising bubbles. Figure 4 shows the local particle velocity and points out the areas where solids lock in frictional contact at very low velocity (marked by the nondimensional velocity $\tilde{v} < 10$, $\tilde{v} = v/d_p f$, i.e., the displacement per pulse measured in particle diameters). In every pulse, as the gas velocity increases, a horizontal channel forms at the bottom, spanning the entire width of the bed. When the gas velocity reaches its maximum at $\varphi \sim 0.5\pi$, the bed is fully expanded and accelerating upwards, but, as the gas velocity decreases, the bed loses inertia and eventually collapses at $\varphi \sim 1.2\pi$ when the gas velocity drops below u_{mf}. Solids are then collected at the distributor forming a large static region, see ⓿ in Figure 4, and the horizontal channel breaks into a new set of bubbles. When the gas velocity increases again, the circulation of powder around each bubble converges onto a single point in between a new pair of rising bubbles, creating a compressed region or pivot that limits the mobility of the solids and stabilizes the axial motion of the bubbles, see ❶ in Figure 4. The solid circulation into the wake of each bubble creates another dense structure, see ❷ in Figure 4, where particles lock in friction, transmitting a compressing stress onto the

distributor that will be responsible for the alternation of the nucleation sites in the next pulse [45], creating the final pattern.

From the above it is clear that, qualitatively, the formation of the pattern stabilizes the bubble motion and restricts the ability of the solids to traverse the bubble wakes, which is discussed further in Section 5.3. What follows is an evaluation of how this phenomenon affects the circulation of the solid phase and its lateral mobility. The smallest possible realization of this phenomenon is studied, consisting of the formation of approximately 1.5 bubbles in each pulse, i.e., a single full bubble and a smaller half bubble forming at one of the walls (see Figure 4). Mixing will be studied by dividing the bed laterally in compartments delimited by the lateral positions of these bubbles. The boundaries of the compartments are calculated as the mean position of the trajectories of the full central bubbles, which, in this case, results in two vertical paths (one full bubble every pulse). The average lateral positions of both trajectories mark the boundaries x_1 and x_2 of the compartments. Figure 5 shows an example of the bubble positions for cases 5, 6 and 7 Hz. One observes much more variability in the structured flows for the 6 Hz and 7 Hz cases, where bubble trajectories do not seem as stable as for the 5 Hz case. The central compartment in the 5 Hz case has a span equal to half of the pattern wavelength (distance between two full bubbles in a larger pattern) and it roughly represents the space between one side of a bubble and its neighboring central pivot (region ❶ in Figure 4). The system is symmetrical with the central compartment appearing perfectly centered, and yet wider (3.73 cm) than the side compartments (3.14 cm) meaning that, for 5Hz pulses, the computational domain is not wide enough to accommodate two complete half bubbles at the walls. The implications of this will be discussed further in Section 5.3.

The particles inside a compartment $x_1 \leq x \leq x_2$ are marked and their positions tracked in time to evaluate their dispersion into the rest of the bed. An effective lateral dispersion coefficient is calculated using the approach given in Section 4, for fluidized beds oscillating at different pulsation frequencies (5, 6, 7 Hz), as well as for a bed operated at a constant gas flow rate.

5.2. LATERAL DISPERSION

Results from simulations and experiments are compared in Table 2. CFD-DEM simulations can provide an accurate representation of the gas dynamics in the system, showing quantitative agreement in the prediction of bubble size and separation in constant and oscillating systems at all frequencies. Although the values of bubble size and separation are well predicted, it is clear that the stability of the flow structure in the experiments at 6 Hz and 7 Hz is not captured in the simulations. A stable pattern is responsible for the low values of the experimental standard deviations of the bubble size and wavelength in Table 2 and Figure 5. The simulations show a much higher level of lateral bubble mobility and a larger variability in size throughout the pulse. In the case of constant flow (f = 0 Hz) in Table 2, the bubble diameter in the simulations is 28 % larger than in experiments, simply because of the difference in the reference minimum fluidization velocity used for the experimental and the computational cases. Both experiments and simulations are run at a superficial gas velocity $u = 2.5u_{mf}$, and given that the computational minimum fluidization velocity is larger than in the experiments, a larger gas volume is available for bubble formation.

The following sections analyze the solid mixing behavior for each case.

5.2.1. Constant gas flow

Lateral dispersion in bubbling beds has been widely studied both experimentally [17–21] and numerically [16,22–24]. As a benchmark for the verification of the model and comparison with the oscillating beds, a bubbling bed at constant gas flow is simulated. A common reference is used, setting the gas inlet velocity to 2.5 times the minimum fluidization u_{mf}. As expected, this leads to bubbles with a wide size distribution and a chaotic spatial distribution. An effective lateral dispersion coefficient is derived according to the procedure in Section 4, where the particles within a selected region $x_1 \leq x \leq x_2$ are marked, and the concentration of these so-called tracer particles is monitored in time. The average concentration, $C_{t,av}$, is calculated as described in Section 4 and is normalized for simplicity by the maximum initial tracer concentration over all lateral positions. Its time evolution is shown in Figure 6. Fitting to Eqn. (28) yields a lateral dispersion coefficient of 1.473 x 10^{-4} m² s^{-1}. Figure 6 shows $C_{t,av}$ associated to the dispersion observed in CFD-DEM simulations (circles) and the corresponding fit to the theoretical model (red line), described by Eqn. (28). Fits using different dispersion coefficients (dashed lines) are added to illustrate the range of error in fitting. This error is related to the short time scale oscillations observed in the evolution of the average concentration, which are related to, on the one hand, fluctuations in the bed density and, on the other hand, rapid exchange of particles in and out of the tracked compartment.

The above methodology differs in three aspects from the one usually applied in literature. First, as already briefly discussed in Section 4, a strict definition of concentration is used, as opposed to the void-free concentration or mass fraction commonly found in literature [16,22,23]. The two approaches are only equivalent when the bed density is uniform, which is not the case in a bubbling bed. Using the void-free tracer concentration results in an artificial smoothing of the evolution of the concentration, see Figure 7a versus Figure 7b. A second difference is related to the initial

condition. In the pulsed flow cases, one must start from a dynamic condition, meaning that the bed is already moving at the beginning of particle tracking. Starting at another point in time would result in a slightly different value for the dispersion coefficient; thus, many initial points are needed to obtain an average D_{sr}.

The value of the fitted dispersion coefficient does not depend on the chosen values for x_1 and x_2. By tracking half of the bed under a constant gas flow, i.e., using $x_1 = 0, x_2 = W/2$, as is typically done in literature (Figure 7a), a comparable, only slightly lower value for the lateral dispersion coefficient is obtained. This agrees with the observations by Berruti et al. [48], who point to spatial non-uniformities in the particle mixing behavior that cause the lateral dispersion coefficient to vary, depending on the position in the bed with respect to the walls. However, given the variability in the evolution of D_{sr} (which can only be observed with the present definition of concentration), the difference between the two results lies within an acceptable error margin. The values obtained for D_{sr} are on the same order of magnitude as values calculated using the correlations of Shi and Fan [21], Berruti et al. [48] and Borodulya et al. [19], as shown in Figure 8.

5.2.2. Periodically pulsating gas flow

The pulsed cases are analyzed following the same procedure. Particles in the central compartment corresponding to the lateral positions $x_1 \leq x \leq x_2$ given in Figure 5 are marked and their positions are monitored over time. Fitting the decay of $C_{t,av}$ to the expression in Eqn. (28) allows us to determine the lateral dispersion coefficients. Table 3 provides a summary of the compartments used and the resulting effective dispersion coefficients for constant and pulsed beds, and Figure 8 compares them with available correlations. The bed operated at a constant flow and

the beds pulsed at 6 Hz and 7 Hz all show lateral dispersion coefficients in quantitative agreement with the expectation for typical bubbling beds. The structured bed at 5 Hz, however, shows an effective diffusion coefficient 3-5 times lower than that of a bed operating at the same conditions without the oscillation. This abnormal behavior is linked to the compartmentalization of the solid flow. As will be discussed in the next section, the compartmentalization makes dispersion in these structured beds different from a diffusion-driven process. Hence, the effective diffusion coefficients in Table 3 are ill-defined and should be regarded solely as illustration for comparison with literature on unstructured beds.

Figure 9 shows the initial state and the resulting mixing of a set of tracer particles, comparing the cases at a constant flow and at a gas pulsation of 5 Hz. Note that the tracer particles were initially marked during the nucleation of a new set of bubbles, at $\varphi \sim 0.8\pi$. The tracer particles are colored black, while the remaining ones are colored grey. In the traditional bed the solids quickly disperse through the bed, whereas in the structured bed dispersion is much slower and shows a clear anisotropy. The outflow of particles from the middle compartment in the structured bed is not random. It occurs at the bottom of the bed, and it is driven by the nucleation phase of the process. The tracer particles leave the compartment via the bottom during periodic bursts. A horizontal channel forms at the bottom of the bed during the nucleation phase ($0.6 < \varphi < 1.2\pi$) and it breaks into two bubbles when the bed collapses after the drop of the gas velocity below u_{mf} ($\varphi \sim 1.2\pi$) [45]. One of these bubbles flows to the boundary of the compartment (left or right in alternate pulses) and the other one flows further away, in the opposite direction. The reconfiguration of the channel into bubbles pushes the tracer particles towards the bottom plate and out of the compartment in a different direction every pulse. The compartment is then

replenished with an influx of (non-tracer) particles entering via the top in every defluidization cycle.

Table 2 shows that mixing improves at higher pulsating frequency. Faster oscillations create smaller bubbles and reduce the amount of time that the bed defluidizes. The simulations at 6 and 7 Hz reproduce a bubble pattern, but the size and lateral mobility of the bubbles is much larger than in the experiments or the oscillations at 5 Hz. This results in a breakdown of the fully correlated solid recirculation, creating faster mixing. The next section describes the link between the reduction in effective lateral dispersion coefficient, the coordinated motion of bubbles and the compartmentalization of the solid flow in the case at 5 Hz. This may also be applicable to higher pulsation frequency but the lack of accuracy in the 6 Hz and 7 Hz simulations does not allow to explore it further.

5.3. COMPARTMENTALIZATION

The compartmentalization is intimately linked to the solid-like structures formed during the oscillation. Figure 10 illustrates this phenomenon with the recirculation patterns observed in the bed and Figure 11 provides quantification, by reporting the decay of the average concentration in the monitored compartment as a function of time for the structured case at 5 Hz.

Figure 10 shows the local particle velocity, marking regions of very low velocity and the areas of the bed with positive or negative axial velocity v_z and lateral velocity v_x. When the gas superficial velocity drops below u_{mf}, two new bubbles are formed, and the collapsing bed creates a pile of defluidized powder in between the two former bubbles. When the gas velocity increases again, this dense structure, see ⓿ in Figure 4 and Figure 10, breaks. In the area between the existing bubbles, ❶ in Figure 4 and Figure 10, the advancing front is pushed against a collapsing bed and the solids converge to a single point at the tip of the pile. The high solids concentration redirects

the gas flow into the existing bubbles, which breaks up the dense bottom structure into two identifiable regions: a rhomboid at the top and another in the wake of the existing bubbles, ❷ in Figure 4 and Figure 10. In the latter, the solid flow converges, pushing down a new pile onto the distributor and flowing up into the bubble. During the bubbling phase ($1.2 < \varphi < 2.1\pi$), the solids pushed aside into the central region at the top of the bed cannot flow across the trail of the previous bubbles delimited by the position of the central pivot ❶, nor can they flow across the wake of the existing bubbles to the other side. This results in the formation of a fixed compartment between the bubble and the pivot with an influx rate of particles at the top and an axial downward flow. At the bottom, however, there is an exit rate. The powder contained into the central region is moved aside into the bubble wake first, and then pushed upwards, creating a twin neighboring compartment with an upwards flow. Figure 10 illustrates the recirculation loops created as visible areas of positive or negative lateral velocity v_x (green/orange, right images in Figure 10). They are formed when the bubbles are nucleated and remain stable throughout the pulsation. When the bubbles break up at the freeboard ($\varphi \sim 2.2 - 2.4\pi$) the bed is already fully expanded, but the solid recirculation loops survive intact.

Lateral mixing in a periodically structured bed shows not only a quantitative difference, but also a qualitative difference to the behavior of a traditional bubbling bed. A structured system cannot be assimilated into a 1D diffusion-like process. The evolution of the concentration given in Figure 11a corresponds to a 1D advection-diffusion process, whereby $C_{t,av}$ initially drops linearly, as a result of a constant outflow rate, with an average net advection rate $\overline{r_c}$. An interesting phenomenon is observed in the evolution of $C_{t,av}$ related to recirculation. On top of the small-scale fluctuations owing to the rapid exchange between neighboring compartments, a structured bed shows also a much larger scale fluctuations with a period of approximately 8 s (secondary peaks in Figure 11a),

indicative of long-range recirculation in the bed. Figure 11b and c show examples of the trajectories responsible for the secondary peaks in Figure 11a, created by particles that come back to their original (middle, grey) compartment after having exited and having passed through the left or right neighboring compartments. Particles leave the central compartment near the bottom and flow into the bottom of the neighboring compartments. Here, the interaction with the bubbles causes them to gradually move upwards. Once they reach the top, they can be pushed back to the central compartment again, or further in the opposite direction into a next compartment (or, in this case, the side wall). In the present simulations, the side wall replaces the role of a second-neighboring compartment. Particles near the wall travel down to the bottom where they are pushed to the center again and start moving upwards under the influence of the bubble column. It is intuitively clear that the solid axial flow in neighboring compartments has an opposite direction. The time for making a complete rotation in one of the loops shown in Figure 11b and c is approximately 8 s, which marks the period of the long-range fluctuation of the concentration in Figure 11a. Macromixing is, therefore, purely governed by the interaction between neighboring compartments through multiple repetitions of the same recirculation loop. It is worth noting that the characteristic size of the loop (i.e., half of the bubble separation or wavelength) is constant throughout a structured bed, where all bubbles maintain the same separation. This observation has two important consequences: it leads to homogenization of the system, and it enables direct external control. The size of the compartment and the recirculation loop could be modified externally by simply manipulating the characteristics of the pulsation, namely the frequency, the amplitude, and the minimum flowrate.

Figure 12 shows the same analysis in beds oscillating at 6 Hz and 7 Hz. Increasing the frequency results in smaller bubbles and/or multiple arrays. As described before, under the investigated

conditions the experimental bubble pattern can be reproduced for 6 Hz and 7 Hz, but with higher instability. Consequently, the recirculation areas described earlier are no longer stable and lateral dispersion increases. Mixing is no longer dominated by long-range circulation and the overall effective dispersion coefficient complies with expectations for a fluidized bed at constant flowrate, see Table 2 and Figure 8. However, the evolution of the concentration reveals that it is not a purely diffusion-dominated process, indicating that even an unstable pattern introduces a certain level of directionality in the solid mixing. The compartmentalization observed here is the full expression of the anomalous sub-diffusive process reported in smaller-scale pulsating beds, which are affected by wall effects [27], when the system is allowed to self-organize and structure dynamically.

This analysis shows that a structured system presents several advantages. It exposes the solids to a well-defined and much narrower history, limited to multiple repetitions of the same single recirculation loop, associated to each bubble nucleation site. Since all bubbles have the same size, the entire population of particles undergoes the same gas-solid contact pattern and the same stress history resulting from particle-particle collisions. To describe this mixing pattern with an engineering model, a compartmental model with advection is clearly more appropriate than a 1D diffusion model. Figure 13 represents the bed as an idealized system of parallel compartments, each consisting of a bubble zone and an emulsion zone interacting with given exchange rates $\bar{r}_{eb}$ and $\bar{r}_{be}$. Figure 13a shows the compartments delimited between the positions of the central pivots and the rising bubbles. In each one, the gas flows upwards, the solids flow axially in alternate directions in neighboring compartments, and exchange mass laterally at a rate $\bar{r}_c$ entering the system either via the top or the bottom. The central compartment shows a downwards flow of particles, and the two recirculation loops associated to the bubbles are shown in Figure 11b and schematically in Figure 13b. In a structured bed, all bubbles are equally sized, meaning the

exchange rate between the bubble and emulsion zone, $\bar{r}_{eb}$ and $\bar{r}_{be}$, are in effect equal, and, as a result, the advection rate $\bar{r}_c$ between neighboring compartments is also balanced.

Figure 14 reports the instantaneous exchange rates as a function of time and phase angle for the structured case at 5 Hz. As expected, the average exchange rates from the bubble to emulsion phase, $\bar{r}_{be}$, and vice versa, $\bar{r}_{eb}$, are balanced, although the latter shows a wider spread. During every cycle, the bubble-emulsion exchange is fastest at $\varphi \sim \pi$, before the defluidization cycle, when bubbles start to rise slowly. The instantaneous outgoing exchange rate r_{out} between neighboring compartments is highest after the gas flow rate reaches its maximal value, because then the movement of new bubbles at the bottom of the bed pushes particles from one compartment into the other. The incoming flux of particles is out of phase with the outgoing flux: the highest incoming exchange rate, r_{in}, occurs when the gas reaches its minimum value, after the bed collapses. The time-averaged values of r_{out} and r_{in}, i.e., $\bar{r}_{out}$ and $\bar{r}_{in}$, are equal, proving that the exchange rate between neighboring compartments is indeed in balance as suggested in Figure 13.

In the investigated system, the side compartments show an upwards movement, but, being smaller in size, they are not able to accommodate a complete bubble on the outer boundary (i.e., the wall). Hence, a truncated loop is created, where particles fall at the walls, depicted schematically in Figure 13b. While this wall effect will always be present when a pattern ends at the wall of any real (wider) bed, it can admittedly have a larger effect on the small system studied here. This wall effect is likely responsible for the slight misalignment observed between the instantaneous positions of the pivots and the average position of the bubble nucleation sites, cf. the alignment of the compartment with the dense area in Figure 13a and Figure 4. Because of the restriction caused by the wall, the position of the central pivots is not strictly constant; it oscillates around the values x_1 and x_2, causing a small error in the definition of the compartment. The effect

gives rise to short-range oscillations in the evolution of the concentration in Figure 11. Therefore, it is important to extend this study to wider structured beds, to understand the interaction between multiple compartments in a single array and implement a full engineering model based on the measurement of residence time distributions in each compartment. Equally, the study of systems with multiple bubble arrays and how compartments would stage vertically remains an open question.

Figure 14 reports the instantaneous exchange rates of particles across the compartments in a bubble pair. The average net advection rate, $\overline{r_c}$, can be calculated through the tracer analysis given in Figure 11. At time t = 0 s, only tracer particles are present in the central compartment, and $\overline{r_c}$ may be computed as the time derivative of $C_{t,av}$, or, in other words, the initial slope of the tracer concentration profile in Figure 11a averaged over several pulsation periods. As such, by averaging over the five initial periods, i.e., over the first second after starting particle tracking, the value of $\overline{r_c}$ is calculated as 3.9 x 10^8 particles m^{-2} s^{-1}, see Table 3. It is worth noting that the $\overline{r_c}$ calculated in this way would differ from the time-averaged values of the instantaneous exchange rates reported in Figure 14, $\bar{r}_{out}$ (or $\bar{r}_{in}$), or, in other words, the derivative of the tracer concentration evolution at time t = 0 s. The detail in Figure 11a illustrates the difference. The time-averaged values $\bar{r}_{out}$ and $\bar{r}_{in}$ include all the fast short-range exchanges of particles between neighboring compartments, due to the particle velocity fluctuations and the oscillation of the position of the compartment as described above. These short-range effects are not included in the average advection rate $\overline{r_c}$.

6. CONCLUSIONS

Lateral mixing in dynamically structured oscillating fluidized beds was investigated using CFD-DEM for varying gas flow pulsation frequencies and compared with that in a traditional bubbling fluidized bed, with constant flowrate. The coordinated motion of the gas bubbles in a structured bed brings the solids into a series of mixing compartments characterized by slow axial mixing and minor lateral interaction. The effective lateral dispersion coefficients are an order of magnitude lower than in a traditional bubbling fluidized bed, but the system is clearly dominated by advection of particles, rather than a 1D Fickian diffusion process. Mixing in a structured bed can be described as a 1D advection process, where macromixing is driven by a long-range lateral circulation of solids that is decoupled from mixing within each compartment. Short-range circulation, or micromixing, is hereby related to local velocity fluctuations within a compartment, originating from the response to the oscillation in the gas flow and independent of the bed geometry. The long-range circulation or macromixing, on the other hand, depends on the domain dimensions. Powder flows through multiple recirculation loops of a constant characteristic size that is a direct function of the wavelength of the bubble lattice. The net average advection rate between the different mixing compartments has been obtained from CFD-DEM simulations. Together with the values for an effective lateral dispersion coefficient, it can be used in engineering reactor models for the design and scale-up of pulsed fluidized bed reactors. In addition to the increase in homogeneity of the system, a structured bed can offer unique advantages in the design of new processes. It is scalable, and the degree of mixing can be controlled independently of the bed design by manipulating the oscillation frequency. Modifying the oscillation, it is possible to control the bubble size and separation that determine the volume of the mixing compartment and the recirculation loop. This may provide the ability to tailor the macroscopic rate of mixing and the

stress history in the powder. Having a way to control these parameters independently can provide new avenues to operate processes with highly exothermic reactions, to make use of thermally sensitive materials requiring control of hot spots in fixed beds, and, particularly, to accurately tailor applications dealing with particle formation or processing, such as coating, where it is crucial to obtain a narrow stress history and uniformity across the final particle product.

In this work, lateral mixing behavior in dynamically structured fluidized beds was demonstrated at a small scale, i.e., for a computational domain consisting of two/three alternating compartments. The future scale-up work must focus on larger-scale computations and establish the interaction between a network of compartments in larger systems, comprising of multiple bubble arrays. This will allow to create a full engineering model of the gas-solid contact pattern in dynamically structured beds, by using axial and lateral interaction rates between a series of compartments.

NOMENCLATURE

Roman

C	Concentration	[m^{-3}]
D_{sr}	Lateral dispersion coefficient	[m^2 s^{-2}]
e	Restitution coefficient	[-]
f	Pulsation frequency	[Hz]
$\boldsymbol{F}$	Force	[N]
$\boldsymbol{g}$	Gravitational acceleration	[m s^{-2}]
G^*	Effective shear modulus	[Pa]
H	Domain height	[m]
$\boldsymbol{I}$	Moment of inertia	[kg m^2]
k	Elastic constant	[N m^{-1}]
m	Mass	[kg]
m^*	Effective particle mass	[kg]
$\boldsymbol{M}$	Momentum exchange	[N m^{-3}]
n	Number	[-]
P	Pressure	[Pa]
R	Particle flux	[particles m^{-2} s^{-1}]
r^*	Effective particle radius	[m]
$\boldsymbol{T}$	Torque	[N m]
$\boldsymbol{u}$	Velocity vector	[m s^{-1}]
u	Velocity magnitude	[m s^{-1}]
V	Volume	[m^3]
W	Width of the bed	[m]
Y	Void free concentration	[-]
Y^*	Effective Young's modulus	[Pa]
Z	Domain thickness	[m]

Greek

β_d	Drag coefficient	[kg m^{-3} s^{-1}]
γ	Visco-elastic damping constant	[N s m^{-1}]

$\boldsymbol{\delta}$	Geometric overlap between paired particles	[m]
ε	Volume fraction	[-]
λ	Bulk viscosity	[Pa s]
μ	Dynamic viscosity	[Pa s]
ρ	Density	[kg m^{-3}]
$\boldsymbol{\tau}$	Stress tensor	[Pa]
ω	Rotational velocity	[rad s^{-1}]

Subscripts/superscripts

A	Amplitude
be	From bubble to emulsion
C	Compartment
eb	From emulsion to bubble
G	Gas
In	Incoming
mf	Minimum fluidization
min	Minimum
N	Normal
Out	Outgoing
P	Particle
R	Relative
T	Tangential, *or,* tracer

Abbreviations

CFD	Computational Fluid Dynamics
DEM	Discrete Element Method

ACKNOWLEDGMENTS

LAV acknowledges financial support from a doctoral fellowship and a travel grant for a long stay abroad from the Fund for Scientific Research Flanders (FWO). The computational work was carried out using the STEVIN Supercomputer Infrastructure at Ghent University, funded by Ghent University, the Flemish Supercomputer Center (VSC), the Hercules Foundation and the Flemish Government – department EWI. The authors would like to thank Dr. Kaiqiao Wu for the provision of experimental data. MOC and VF gratefully acknowledge EPSRC for funding through "Frontier Engineering" and "Frontier Engineering: Progression" Awards (EP/K038656/1; EP/S03305X/1).

ASSOCIATED CONTENT

Supporting information: animations corresponding to the performed simulations.

REFERENCES

[1] M. Rüdisüli, T.J. Schildhauer, S.M.A. Biollaz, J.R. Van Ommen, Scale-up of bubbling fluidized bed reactors - A review, Powder Technol. 217 (2012) 21–38. https://doi.org/10.1016/j.powtec.2011.10.004.

[2] C. Chavarie, J.R. Grace, Interphase mass transfer in a gas fluidized bed, Chem. Eng. Sci. 31 (1976) 741–749. https://doi.org/10.1016/0009-2509(76)80046-2.

[3] J.A. Medrano, F. Gallucci, F. Boccia, N. Alfano, M. van Sint Annaland, Determination of the bubble-to-emulsion phase mass transfer coefficient in gas-solid fluidized beds using a noninvasive infra-red technique, Chem. Eng. J. 325 (2017) 404–414. https://doi.org/10.1016/J.CEJ.2017.05.089.

[4] J.R. van Ommen, J. Nijenhuis, C.M. van den Bleek, M.-O. Coppens, Four Ways To Introduce Structure in Fluidized Bed Reactors, Ind. Eng. Chem. Res. 46 (2007) 4236–4244. https://doi.org/10.1021/ie061318o.

[5] M.-O. Coppens, J.. van Ommen, Structuring chaotic fluidized beds, Chem. Eng. J. 96 (2003) 117–124. https://doi.org/10.1016/J.CEJ.2003.08.007.

[6] M.-O. Coppens, M.A. Regelink, C.M. van den Bleek, Pulsation induced transition from chaos to periodically ordered patterns in fluidised beds, Proc. 4th World Conf. Part. Technol. (WCPT-2002), Pap. 355. (2002) 1–8.

[7] N.G. Deen, M. Van Sint Annaland, M.A. Van der Hoef, J.A.M. Kuipers, Review of discrete particle modeling of fluidized beds, Chem. Eng. Sci. 62 (2007) 28–44. https://doi.org/10.1016/J.CES.2006.08.014.

[8] A. Bakshi, C. Altantzis, R.B. Bates, A.F. Ghoniem, Study of the effect of reactor scale on fluidization hydrodynamics using fine-grid CFD simulations based on the two-fluid model, Powder Technol. 299 (2016) 185–198. https://doi.org/10.1016/J.POWTEC.2016.05.029.

[9] A. Bakshi, M. Shahnam, A. Gel, T. Li, C. Altantzis, W. Rogers, A.F. Ghoniem, Comprehensive multivariate sensitivity analysis of CFD-DEM simulations: Critical model parameters and their impact on fluidization hydrodynamics, Powder Technol. 338 (2018) 519–537. https://doi.org/10.1016/J.POWTEC.2018.06.049.

[10] K. Wu, L. de Martín, L. Mazzei, M.-O. Coppens, Pattern formation in fluidized beds as a tool for model validation: A two-fluid model based study, Powder Technol. 295 (2016) 35–42. https://doi.org/10.1016/J.POWTEC.2016.03.011.

[11] K. Wu, L. de Martín, M.-O. Coppens, Pattern formation in pulsed gas-solid fluidized beds – The role of granular solid mechanics, Chem. Eng. J. 329 (2017) 4–14. https://doi.org/10.1016/j.cej.2017.05.152.

[12] D. Kunii, O. Levenspiel, Gas Dispersion and Gas Interchange in Bubbling Beds, in: Fluid. Eng., Butterworth-Heinemann, 1991: pp. 237–256. https://doi.org/10.1016/B978-0-08-050664-7.50016-0.

[13] W.G. May, Fluidized-bed Reactor Studies, Chem. Eng. Progr. 55 (1959) 49–56. https://ci.nii.ac.jp/naid/10004305274/en/.

[14] W.K. Lewis, E.R. Gilliland, H. Girouard, Heat transfer and solids mixing in a bed of fluidized solids, Chem. Eng. Prog. Symp. Ser. 58 (1962) 87–97.

[15] A. Avidan, J. Yerushalmi, Solids mixing in an expanded top fluid bed, AIChE J. 31 (1985) 835–841. https://doi.org/10.1002/aic.690310520.

[16] O. Oke, B. Van Wachem, L. Mazzei, Lateral solid mixing in gas-fluidized beds: CFD and DEM studies, Chem. Eng. Res. Des. 114 (2016) 148–161. https://doi.org/10.1016/J.CHERD.2016.08.014.

[17] M. Kashyap, D. Gidaspow, Measurements of Dispersion Coefficients for FCC Particles in a Free Board, Ind. Eng. Chem. Res. 50 (2011) 7549–7565. https://doi.org/10.1021/ie1012079.

[18] P. Pandey, R. Turton*, P.Y. And, L. Shadle, Nonintrusive Particle Motion Studies in the Near-Wall Region of a Pilot-Scale Circulating Fluidized Bed, (2004). https://doi.org/10.1021/IE0307737.

[19] V.A. Borodulya, Y.G. Epanov, Y.S. Teplitskii, Horizontal particle mixing in a free fluidized bed, J.

Eng. Phys. 42 (1982) 528–533. https://doi.org/10.1007/BF00824945.
[20] J. Sánchez-Prieto, F. Hernández-Jiménez, L.M. Garcia-Gutierrez, A. Soria-Verdugo, Experimental study on the characteristic mixing time of solids and its link with the lateral dispersion coefficient in bubbling fluidized beds, Chem. Eng. J. 307 (2017) 113–121. https://doi.org/10.1016/j.cej.2016.08.075.
[21] Y. Shi, L.T.T. Fan, Lateral Mixing of Solids in Batch Gas-Solids Fluidized Beds, Ind. Eng. Chem. Process Des. Dev. 23 (1984) 337–341. https://doi.org/10.1021/i200025a026.
[22] O. Oke, P. Lettieri, P. Salatino, R. Solimene, L. Mazzei, Numerical simulations of lateral solid mixing in gas-fluidized beds, Chem. Eng. Sci. 120 (2014) 117–129. https://doi.org/10.1016/J.CES.2014.08.049.
[23] D. Liu, X. Chen, Lateral solids dispersion coefficient in large-scale fluidized beds, Combust. Flame. 157 (2010) 2116–2124. https://doi.org/10.1016/j.combustflame.2010.04.020.
[24] M. Farzaneh, S. Sasic, A.-E. Almstedt, F. Johnsson, D. Pallarès, A novel multigrid technique for Lagrangian modeling of fuel mixing in fluidized beds, Chem. Eng. Sci. 66 (2011) 5628–5637. https://doi.org/10.1016/J.CES.2011.07.060.
[25] T. Shinbrot, F.J. Muzzio, Noise to order, Nature. 410 (2001) 251–258. https://doi.org/10.1038/35065689.
[26] T.H. Metcalf, J.B. Knight, H.M. Jaeger, Standing wave patterns in shallow beds of vibrated granular material, Phys. A Stat. Mech. Its Appl. 236 (1997) 202–210. https://doi.org/10.1016/S0378-4371(96)00370-6.
[27] J.E. Higham, M. Shahnam, A. Vaidheeswaran, Anomalous diffusion in a bench-scale pulsed fluidized bed, Phys. Rev. E. 103 (2021) 43103. https://doi.org/10.1103/PhysRevE.103.043103.
[28] V. Francia, K. Wu, M.-O. Coppens, Dynamically structured fluidization: Intensification of gas-solid fluidized bed operation by using an oscillating gas flow, Chem. Eng. Process. Process Intensif. 159 (2021) 108143.
[29] C. Goniva, C. Kloss, N.G. Deen, J.A.M. Kuipers, S. Pirker, Influence of rolling friction on single spout fluidized bed simulation, Particuology. 10 (2012) 582–591. https://doi.org/10.1016/j.partic.2012.05.002.
[30] OpenFOAM-v5, OpenFOAM Found. Ltd. (2017). https://openfoam.org.
[31] C. Kloss, C. Goniva, A. Hager, S. Amberger, S. Pirker, Models, algorithms and validation for opensource DEM and CFD-DEM, Prog. Comput. Fluid Dyn. An Int. J. 12 (2012) 140. https://doi.org/10.1504/PCFD.2012.047457.
[32] P.A. Cundall, O.D.L. Strack, A discrete numerical model for granular assemblies, Géotechnique. 29 (1979) 47–65. https://doi.org/10.1680/geot.1979.29.1.47.
[33] Y. Tsuji, T. Tanaka, T. Ishida, Lagrangian numerical simulation of plug flow of cohesionless particles in a horizontal pipe, Powder Technol. 71 (1992) 239–250. https://doi.org/10.1016/0032-5910(92)88030-L.
[34] H. Deresiewicz, R.D. Mindlin, Elastic spheres in contact under varying oblique forces, PhD thesis. Columbia University. Department of Civil Engineering, 1952.
[35] H. Jasak, Error Analysis and Estimation for the Finite Volume Method with Applications to Fluid Flows, PhD thesis. University of London, Department of Mechanical Engineering, 1996.
[36] D. Gidaspow, Multiphase Flow and Fluidization, Elsevier, 1994. https://doi.org/10.1016/C2009-0-21244-X.
[37] C.Y. Wen, Y.H. Yu, Mechanics of fluidization, Chem. Eng. Prog. Symp. Ser. 62 (1966) 100.
[38] S. Ergun, Fluid Flow Through Packed Columns, Chem. Eng. Progr. 48 (1952) 89–94.
[39] S.F. Foerster, M.Y. Louge, H. Chang, K. Allia, Measurements of the collision properties of small spheres, Phys. Fluids. 6 (1994) 1108–1115. https://doi.org/10.1063/1.868282.
[40] C.R. Müller, D.J. Holland, A.J. Sederman, S.A. Scott, J.S. Dennis, L.F. Gladden, Granular temperature: Comparison of Magnetic Resonance measurements with Discrete Element Model simulations, Powder Technol. 184 (2008) 241–253. https://doi.org/10.1016/J.POWTEC.2007.11.046.

[41] S. Lommen, D. Schott, G. Lodewijks, DEM speedup: Stiffness effects on behavior of bulk material, Particuology. 12 (2014) 107–112. https://doi.org/10.1016/J.PARTIC.2013.03.006.
[42] Y. Kaneko, T. Shiojima, M. Horio, DEM simulation of fluidized beds for gas-phase olefin polymerization, Chem. Eng. Sci. 54 (1999) 5809–5821. https://doi.org/10.1016/S0009-2509(99)00153-0.
[43] R. Moreno-Atanasio, B.H. Xu, M. Ghadiri, Computer simulation of the effect of contact stiffness and adhesion on the fluidization behaviour of powders, Chem. Eng. Sci. 62 (2007) 184–194. https://doi.org/10.1016/J.CES.2006.08.036.
[44] Y. Gu, A. Ozel, S. Sundaresan, A modified cohesion model for CFD–DEM simulations of fluidization, Powder Technol. 296 (2016) 17–28. https://doi.org/10.1016/J.POWTEC.2015.09.037.
[45] V. Francia, K. Wu, M.-O. Coppens, On the role of energy dissipation in a dynamically structured fluidized bed, Chem. Eng. Sci. Submitted (2021).
[46] M.A. van der Hoef, M. Ye, M. Van Sint Annaland, A.T. Andrews IV, S. Sundaresan, J.A.M. Kuipers, Multi-scale modeling of gas-fluidized beds, Adv. Chem. Eng. 31 (2006) 65–149.
[47] L.E. Silbert, D. Ertas, G.S. Grest, T.C. Halsey, D. Levine, S.J. Plimpton, Granular flow down an inclined plane: Bagnold scaling and rheology, Phys. Rev. E. 64 (2001) 51302. https://doi.org/10.1103/PhysRevE.64.051302.
[48] F. Berruti, D.S. Scott, E. Rhodes, Measuring and modelling lateral solid mixing in a three-dimensional batch gas—solid fluidized bed reactor, Can. J. Chem. Eng. 64 (1986) 48–56. https://doi.org/10.1002/cjce.5450640107.

Table 1: Overview of operating conditions and computational settings.

Gas properties				
Density, ρ_g	1.225 kg m^{-3}			
Viscosity, μ_g	1.8×10^{-5} Pa s			
Particle properties				
Density, ρ_p	2500 kg m^{-3}			
Mean particle diameter, d_p	238 µm			
Young's modulus, Y	10 MPa			
Restitution coefficient, e	0.97			
Poisson's ratio, ν	0.22			
Interparticle friction coefficient, μ_{fr}	0.35			
Particle-wall friction coefficient, μ_w	0.1			
Computational domain				
Bed width, W	0.1 m			
Initial bed height, H_0	0.045 m			
Total domain height, H	0.1 m			
Bed thickness, Z	0.002 m			
Grid dimensions, $n_W \times n_Z \times n_H$	$50 \times 1 \times 50$			
Time step size				
Gas phase	1×10^{-4} s			
Particle phase	1×10^{-6} s			
Gas phase boundary conditions				
Side walls	No-slip			
Inlet	Superficial inlet velocity u $u = u_{min} + u_a[1 + \sin(2\pi f t)]$			
Oscillation frequency, f	Constant	Oscillating		
	0 Hz	5 Hz	6 Hz	7 Hz
Minimum velocity, u_{min}	2.5 u_{mf} (*)		0.0205 m s^{-1}	
Oscillation amplitude, u_a	-		0.0877 m s^{-1}	
Time-averaged velocity, $\overline{u} = u_{min} + u_a$	2.5 u_{mf} (*)		0.1082 m s^{-1}	
Outlet	Fixed pressure, 0 barg			

(*) $u_{mf} = 0.046$ m s^{-1} and 0.056 m s^{-1} for experiments and simulations, respectively.

Table 2: Equivalent bubble diameter, d_{eq}, pattern wavelength, λ, boundaries of the monitored compartment, x_1 and x_2.

f [Hz]	$\overline{u}$ [10^{-2} m s^{-1}]	d_{eq} [10^{-2} m]	λ [10^{-2} m]	x_1 [10^{-2} m]	x_2 [10^{-2} m]
Experimental					
5 Hz	10.82	2.74 ± 0.25	6.84 ± 0.46	n/a	n/a
6 Hz	10.82	1.91 ± 0.32	6.17 ± 0.51	n/a	n/a
7 Hz	10.82	1.53 ± 0.22	3.57 ± 0.57	n/a	n/a
0 Hz	11.5	0.85 ± 0.24	n/a	n/a	n/a
Computational					
5 Hz	10.82	2.80 ± 0.11	7.46 ± 0.15	3.14	6.86
6 Hz	10.82	1.76 ± 0.55	6.06 ± 1.05	1.90	4.92
7 Hz	10.82	1.33 ± 0.47	4.49 ± 1.60	5.76	7.99
0 Hz	14.0	1.20 ± 0.43	n/a	0	5.0
0 Hz	14.0	1.20 ± 0.43	n/a	3.13	6.86

Table 3: Compartments, effective lateral dispersion coefficients and advection rate.

f [Hz]	$\overline{u}$ [10^{-2} m s^{-1}]	x_1 [10^{-2} m]	x_2 [10^{-2} m]	D_{sr} (*) [10^{-4} m^2 s^{-1}]	D'_{sr} (*) [10^{-4} m^2 s^{-1}]	$\overline{r_c}$ [particles m^{-2} s^{-1}]
5 Hz	10.82	3.14	6.86	0.302	0.306	3.9×10^8
6 Hz	10.82	1.90	4.92	0.626	0.432	n/a
7 Hz	10.82	5.76	7.99	0.788	0.901	n/a
0 Hz	14.0	0	5.0	1.047	1.053	n/a
0 Hz	14.0	3.13	6.86	1.473	1.612	n/a

(*) These effective lateral dispersion coefficients are for comparison purposes only. They are not to be used in combination with the advection rate.

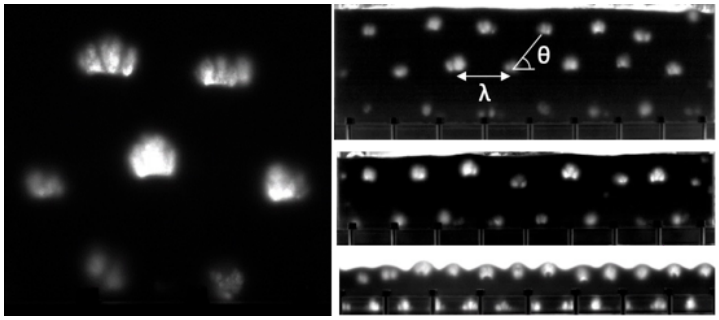

Figure 1: Thin bed of glass beads fluidized with an oscillating air flow showing regular, subharmonic bubble patterns of different scale, characterized by their bubble size, tessellation angle θ and horizontal wavelength λ.

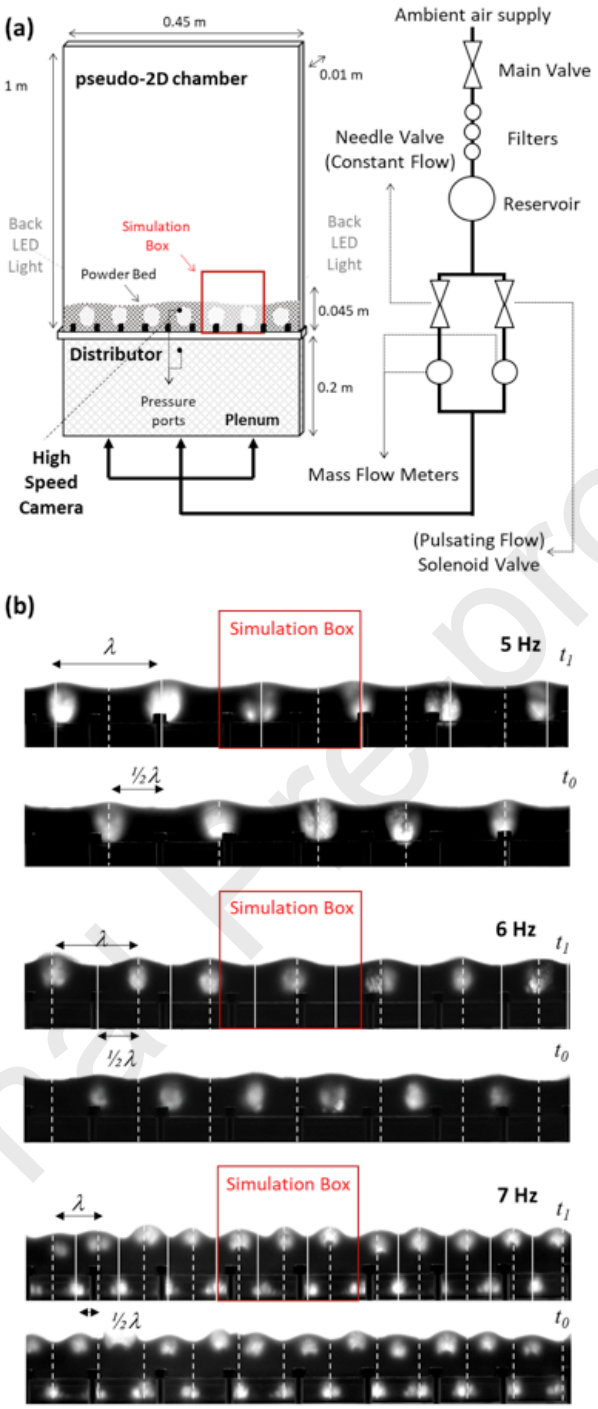

Figure 2: (a) Experimental setup of an oscillating thin fluidized bed. (b) Snapshots of experimental results for two consecutive pulses, t_0 and t_1, at frequencies of 5, 6 and 7 Hz; λ denotes the wavelength. Scale of the simulation box is marked in red.

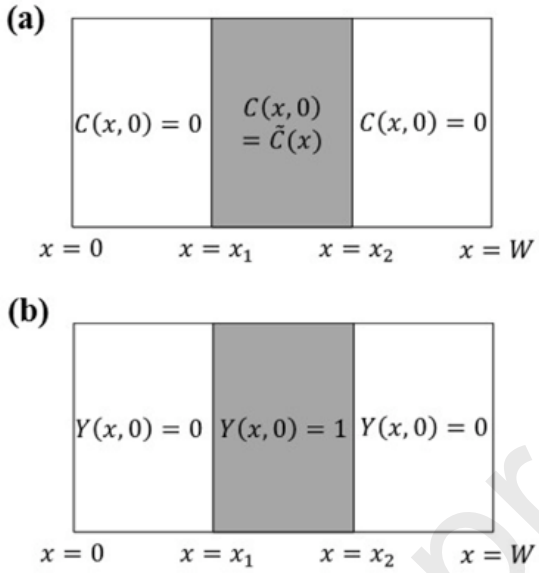

Figure 3: Schematic representation of the initial state of the bed, using (a) the actual concentration of tracer particles [particles m^{-3}], and (b) the void-free concentration of tracer particles [-].

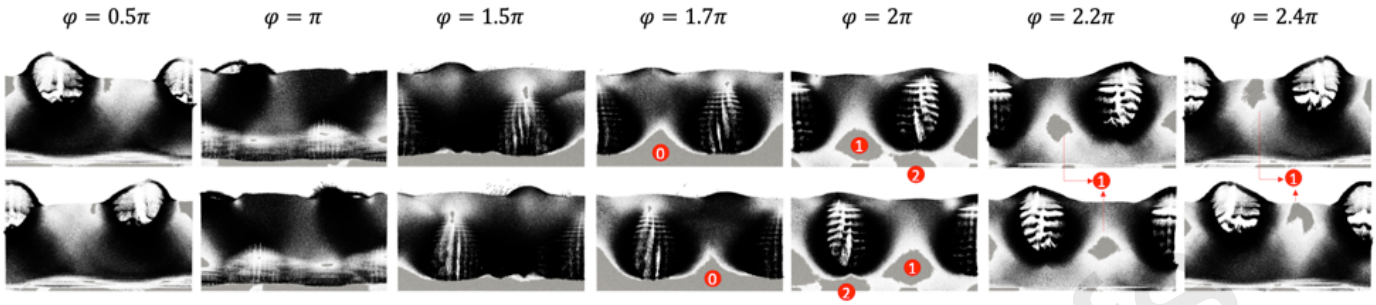

Figure 4: Snapshots of the simulated bubble pattern for increasing phase angle φ in two consecutive periods (top and bottom) for a pulsating gas at 5 Hz. Black velocity vectors for all particles with $\tilde{v} = {}^{v}/(d_p f) > 10$. Particles with $\tilde{v} < 10$ are marked as static in grey.

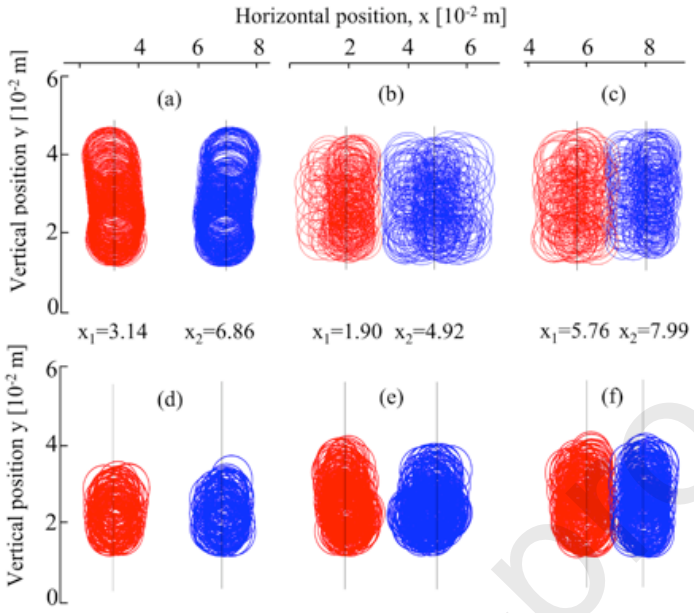

Figure 5: Examples of bubble positions in alternate pulses. Top: obtained from image post-processing of the CFD-DEM results. Bottom: experimental data. (a, d) 5 Hz, (b, e) 6 Hz, (c, f) 7 Hz. Only fully formed bubbles are shown, i.e., bubbles for which the axial position of the center y > 1.75 x 10^{-2} m, for a range of x positions that identifies the bubbles nucleated in alternate pulses.

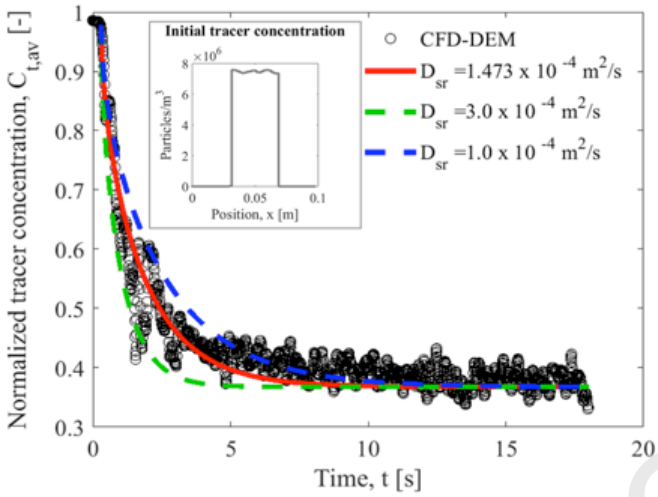

Figure 6: Average, normalized tracer concentration $C_{t,av}$ [-] in the monitored part of the bed ($x_1 \leq x \leq x_2$) as a function of simulation time, for the constant flow case. The boundaries are $x_1 = 3.13 \times 10^{-2}$, $x_2 = 6.86 \times 10^{-2}$ m. The circles indicate the CFD-DEM results, while the lines indicate the theoretical average tracer concentration resulting from the solution of Eqns. (21),(23)-(24) with the indicated dispersion coefficient D_{sr}. The figure insets show the initial tracer concentration profile.

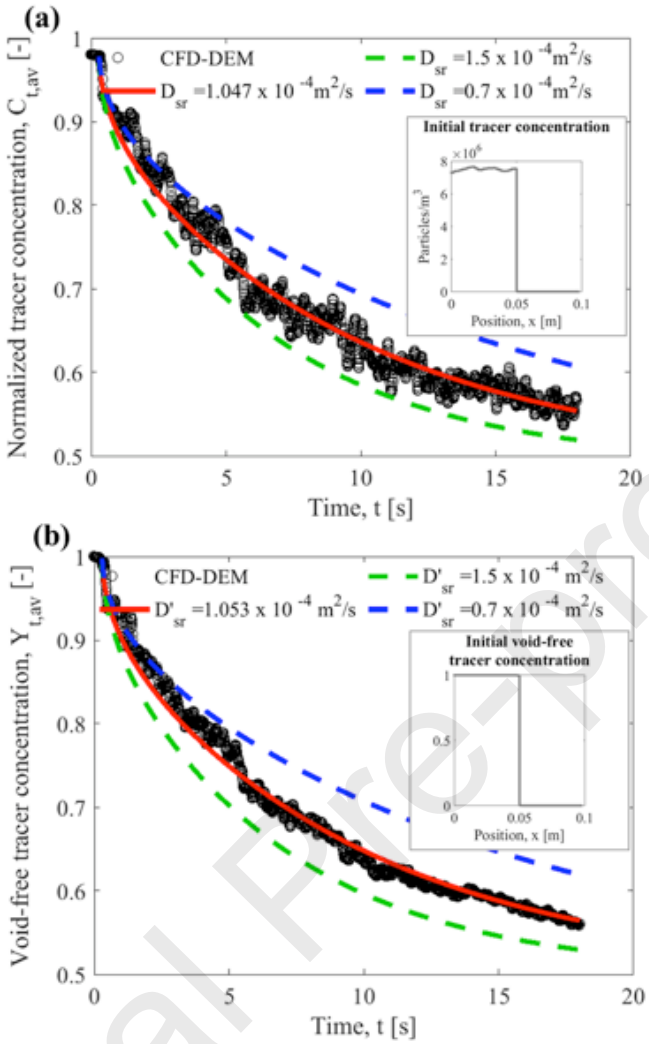

Figure 7: (a) Average normalized tracer concentration $C_{t,av}$ [-] and (b) average void-free tracer concentration $Y_{t,av}$ [-] in the monitored part of the bed ($x_1 \leq x \leq x_2$) as a function of simulation time, for the constant flow case. The boundaries are $x_1 = 0$, $x_2 = 5.0 \times 10^{-2}$ m. The circles indicate the CFD-DEM results, while the lines indicate the theoretical average resulting from the solution of, respectively, Eqns. (21), (23)-(24) and Eqns. (30)-(32) with the indicated dispersion coefficients, D_{sr} and D'_{sr}. The figure insets show the initial concentration profile.

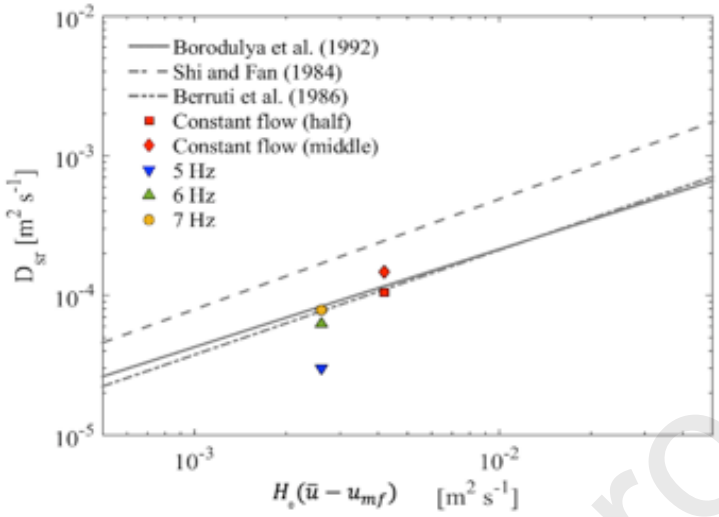

Figure 8: Comparison of lateral dispersion coefficients according to 1D Fickian diffusion fitted in this work with correlations available in literature by Shi and Fan [21], Berruti et al. [48] **and Borodulya et al. [19]. The simulated u_{mf} was used in this analysis.**

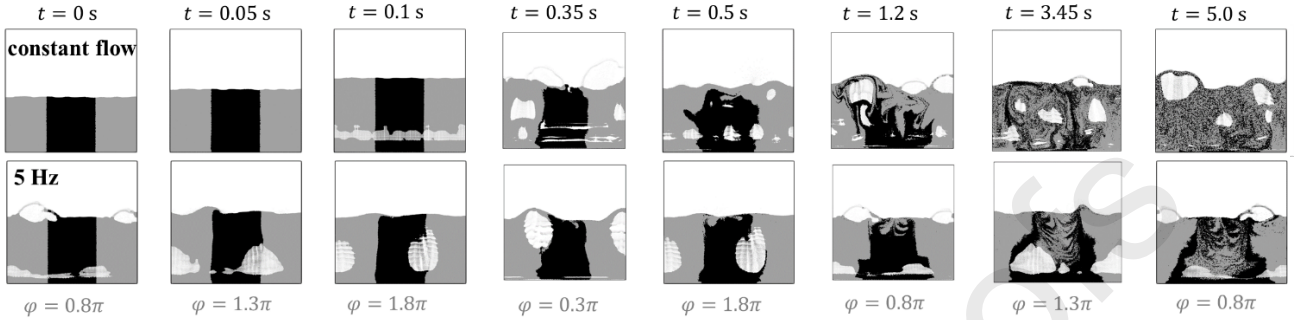

Figure 9: Snapshots of the particle bed at (top) a constant superficial gas inlet velocity, and (bottom) an oscillating flow at 5 Hz, see conditions in Table 1. Initially, a region in the middle of the bed is marked as tracer particles between $x_1 = 3.13 \times 10^{-2}$ m and $x_2 = 6.86 \times 10^{-2}$ m.

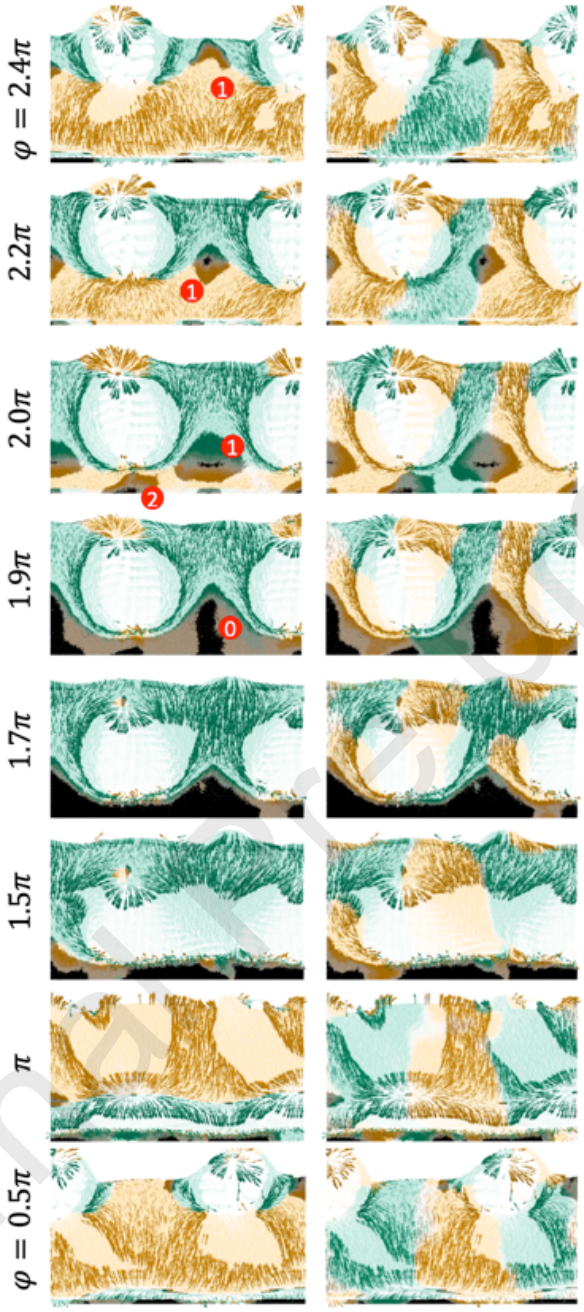

Figure 10: Compartmentalization. Local particle velocity (left: axial velocity v_z, right: lateral velocity v_x) as a function of phase angle. Low velocity areas are marked as particles: $\tilde{v} = v/(d_p f) < 1$ (black), $1 < \tilde{v} < 10$ (color). High velocity areas are marked with vectors, for particles with $10 < \tilde{v} < 100$ (color) and $\tilde{v} > 100$ (white, scaled down x 4). Color indicates direction of velocity components (orange $v > 0$, green $v < 0$). Conditions from Table 1, for an oscillating flow at 5 Hz.

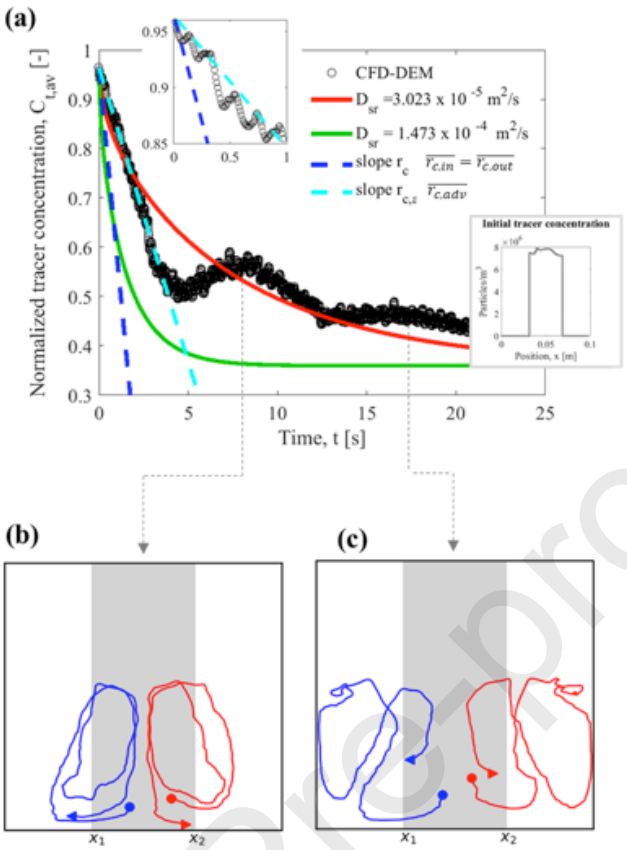

Figure 11: Compartmentalization, when pulsating the gas at 5 Hz. (a) Average scaled tracer concentration $C_{t,av}$ [-] in the monitored section ($x_1 \leq x \leq x_2$) as a function of simulation time. The circles indicate the CFD-DEM results; lines indicate the theoretical $C_{t,av}$ resulting from the solution of Eqns. (21), (23) and (24) with the least-squares fitted dispersion coefficient (red) and with the dispersion coefficient for the constant flow case (green). The figure inset shows the initial value. (b) and (c) Solids circulation: trajectories of sets of individual particles with the bullet indicating the starting position at time t = 0 s, and the triangle indicating the position at t = 20 s. Particles return to the initial compartment after one (b) or two (c) long-range circulations periods or ~8 s. The grey zone corresponds to the monitored section. Conditions from Table 1, for an oscillating flow at 5 Hz.

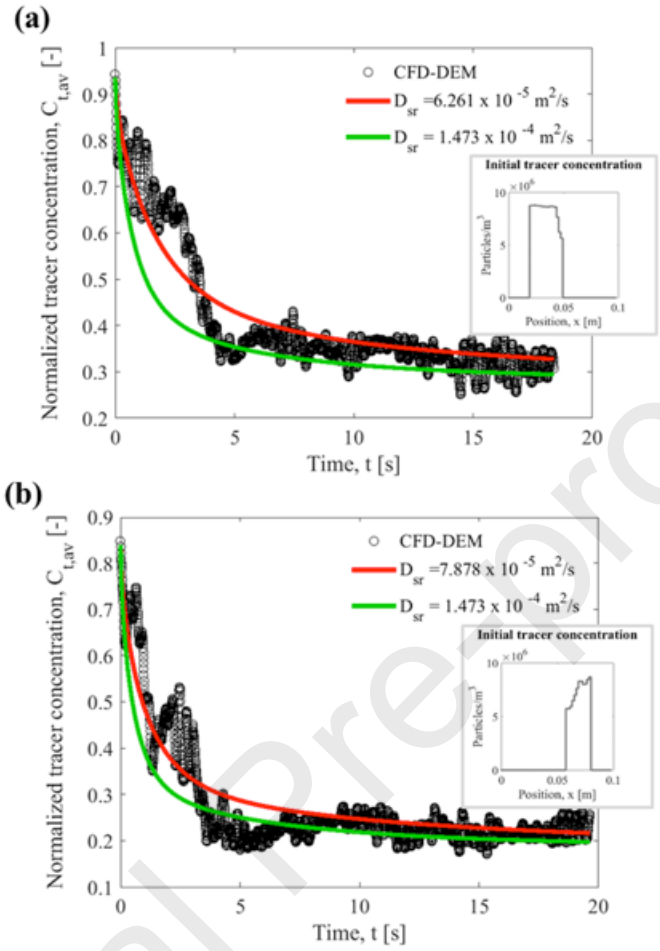

Figure 12: Average normalized tracer concentration $C_{t,av}$ [-] in the monitored section ($x_1 \leq x \leq x_2$) as a function of simulation time, when pulsating the gas supply at 6 Hz (a) and 7 Hz (b). For nomenclature, see Figure 11.

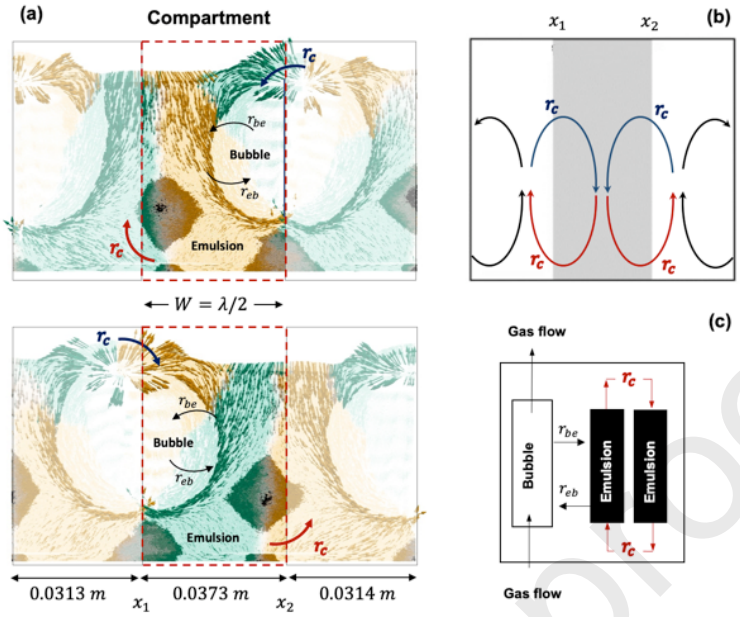

Figure 13: (a) Monitored region, with alternation of the bubble sites in two consecutive pulses and associated rates. For key to velocity map, see Figure 10. (b) Solid circulation across compartments. (c) Simplified surrogate model for a dynamically structured fluidized bed.

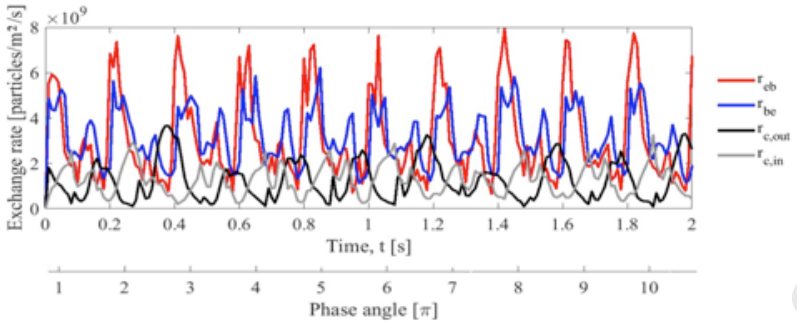

Figure 14: Advection in a structured flow when pulsating the gas supply at 5 Hz: instantaneous exchange rates between the compartments as a function of time.

Highlights

- Dynamically structuring a fluidized bed compartmentalizes the solids circulation.
- Effective solid lateral dispersion coefficients decrease tenfold in structured bed.
- Dispersion in a structured bed is driven by advection and is not diffusion-like.
- Compartmentalization decouples the time scales of macro- and micromixing.
- Mixing compartments interact through a unique and controllable circulation loop.